The generation of magnetic fields by the Biermann battery and the interplay with the Weibel instability.

K. M. Schoeffler,[1] N. F. Loureiro,[1,2] R. A. Fonseca,[1,3] and L. O. Silva[1]

[1] *Instituto de Plasmas e Fusão Nuclear, Instituto Superior Técnico, Universidade de Lisboa, 1049-001 Lisboa, Portugal*

[2] *Plasma Science and Fusion Center, Massachusetts Institute of Technology, Cambridge MA 02139, USA*

[3] *DCTI/ISCTE—Instituto Universitário de Lisboa, 1649-026 Lisboa, Portugal*

An investigation of magnetic fields generated in an expanding bubble of plasma with misaligned temperature and density gradients (driving the Biermann battery mechanism) is performed. With gradient scales L, large-scale magnetic fields are generated by the Biermann battery mechanism with plasma $\beta \sim 1$, as long as L is comparable to the ion inertial length d_i. For larger system sizes, $L/d_e > 100$ (where d_e is the electron inertial length), the Weibel instability generates magnetic fields of similar magnitude but with wavenumber $k d_e \approx 0.2$. In both cases, the growth and saturation of these fields have a weak dependence on mass ratio m_i/m_e, indicating electron mediated physics. A scan in system size is performed at $m_i/m_e = 2000$, showing agreement with previous results with $m_i/m_e = 25$. In addition, the instability found at large system sizes is quantitatively demonstrated to be the Weibel instability. Furthermore, magnetic and electric energy spectra at scales below the electron Larmor radius are found to exhibit power law behavior with spectral indices $-16/3$ and $-4/3$, respectively.

I. INTRODUCTION

The origin of magnetic fields starting from unmagnetized plasmas is a central question in astrophysics. Although much of the observable universe is magnetized such that the magnetic field plays an important role in the dynamics, in the early universe this was not so. During the period before recombination, when the cosmic microwave background was generated, it is widely accepted that there was no magnetic field[1]. Magnetic field growth is generally attributed to the turbulent dynamo[2,3], which greatly amplifies a required initial seed field. The Biermann battery mechanism[4], in contrast, generates magnetic fields in the absence of a seed via perpendicular density and temperature gradients, and is thought to be the major source of these seed fields. The Biermann mechanism can explain the generation of a $\sim 10^{-20} G$ field after recombination, but it is questionable whether turbulent dynamo growth alone can explain amplification up to the $10^{-6} G$ fields seen today throughout the interstellar medium[1], (where the magnetic pressure is of the order of the plasma pressure, $\beta \equiv 8\pi P/B^2 \sim 1$). A possible solution to this problem may be provided by the potential role played by kinetic instabilities in the amplification of magnetic fields. One such instability is the Weibel instability[5], which we will discuss later.

The Biermann mechanism is also the presumed cause of self-generated magnetic fields (of order $10^6 G$, $\beta \sim 1$) found in laser-solid interaction experiments [6–8]. The laser generates an expanding bubble of plasma by hitting and ionizing a solid foil of metal or plastic. This bubble thus has a temperature gradient perpendicular to the beam (hottest closest to the beam axis), and a density gradient in the direction normal to the foil, allowing for the Biermann battery to take place. These experiments, in addition to being interesting in themselves and in inertial confinement fusion, provide an opportunity to help clarify poorly understood astrophysical processes, namely magnetic field generation and amplification, and even turbulence at both fluid and kinetic scales. Temperature gradients form perpendicular to astrophysical shocks (hotter in the center of the shock), while density gradients form parallel to the shock, once again allowing the Biermann battery to take place.

Inspired by the laser-plasma configuration, we investigated, in a previous paper[9], the generation and amplification of magnetic fields using particle-in-cell (PIC) simulations of an expanding plasma bubble with perpendicular temperature and density gradients. These kinetic simulations confirmed the fluid prediction of the Biermann battery[10–12] with the generation and saturation of magnetic fields scaling as $1/L$ for moderate values of $L/d_i > 1$, where d_i is the ion inertial length, and L is the system size. In addition, we found that, for large L these simulations revealed the Weibel instability, which is kinetic in nature, as the major source of magnetic fields, allowing the magnetic field to remain finite ($\beta \sim 1$) for large L. We will hereupon refer to Ref.[9] as Paper I.

In the present paper a more in-depth study of this problem is performed. In the following sections we further detail and expand the results of Paper I[9], showing the scaling of Biermann generated magnetic fields with system size, and the formation of the Weibel instability for large system sizes ($L/d_e > 100$). In the next two sections we show the theory behind the two mechanisms for magnetic field growth; the Biermann battery mechanism (section II) and the Weibel instability (section III). Section IV describes the computational setup. In section V we provide evidence that the results from Paper I[9] hold for larger, more realistic, mass ratios. In Section VI we

show further agreement between observations of the instability in the large L/d_e regime and theoretical predictions of the Weibel instability. In Section VII we present agreement with gyrokinetic theory via power law slopes of both the magnetic and electric field energy. Finally, in section VIII we reiterate the importance of the $1/L$ scaling of Biermann magnetic fields, and the existence of the finite Weibel magnetic fields ($\beta_e \sim 1$) generated in large scale temperature and density gradients, relevant for both astrophysical systems and some current and future laser setups.

II. BIERMANN BATTERY

Assuming a two-fluid description of a plasma with massless electrons, the magnetic field evolution is given by the generalized induction equation,

$$\frac{\partial \boldsymbol{B}}{\partial t} = \boldsymbol{\nabla} \times (\boldsymbol{v} \times \boldsymbol{B}) + \frac{\eta c^2}{4\pi}\nabla^2 \boldsymbol{B} - \frac{1}{en}\boldsymbol{\nabla} \times (\boldsymbol{j} \times \boldsymbol{B}) \\ - \frac{c}{ne}\boldsymbol{\nabla} n \times \boldsymbol{\nabla} T_e, \quad (1)$$

which shows the evolution of magnetic field $\boldsymbol{B}$, based on the fluid velocity $\boldsymbol{v}$, the current density $\boldsymbol{j} = c\boldsymbol{\nabla} \times \boldsymbol{B}/4\pi$, the number density n, and the electron temperature $T_e \equiv P_e/n$, where P_e is the electron plasma pressure. Here, c is the speed of light, η is the resistivity, and e is the charge of an electron. The terms on the RHS of Eq. (1) from left to right are the convective term, the resistive term, the Hall term, and the Biermann battery term. The induction equation is often simplified by assuming the system size L is large compared to all kinetic scales, and only considering the convective term on the RHS. The resistive term compared to the convective term scales as δ_R/L where $\delta_R \equiv \eta c^2/4\pi v$ is the resistive scale, the Hall term as $(d_i/L)(v_A/v)$ where v_A is the Alfvén velocity, and the Biermann battery term as $(\rho_e/L)(v_{the}/v)$ where ρ_e is the electron Larmor radius, and v_{the} is the electron thermal velocity. In ideal magnetohydrodynamics (MHD), all of these terms are neglected because δ_R, d_i, and ρ_e are assumed small compared to L.

The Biermann battery term operates when the density and the temperature gradients are not parallel to each other ($\boldsymbol{\nabla} n \times \boldsymbol{\nabla} T_e \neq 0$). Although in MHD it is a small term, it is the only term independent of $\boldsymbol{B}$ and thus dominates for small magnetic fields (where $\rho_e > L$).

Starting with $\boldsymbol{B} = 0$, all terms on the RHS except for the Biermann term can be ignored, and thus $\boldsymbol{B}$ grows linearly. Based on scaling, given $T_e = m_e v_{the}^2$, we find:

$$B(t) \approx \frac{m_e c}{e}\frac{v_{the}^2}{L_T L_n}t, \quad (2)$$

where L is more precisely defined by the length of the gradients ($L_n \equiv n/\nabla n$, $L_T \equiv T_e/\nabla T_e$, which we will take to be comparable). Assuming the other RHS terms remain small, the linear growth should continue until the Biermann term disappears: within an electron transit time L_T/v_{the}, hot electrons flow down the temperature gradient, while cold electrons flow up, smoothing out the gradient, and effectively removing the Biermann term. (Note, the density gradient, on the other hand smooths out at the much slower sound transit time L_n/c_s, where $c_s \equiv \sqrt{T_e/m_i}$ is the sound speed.) Because the gradient changes with time, the magnetic field growth eventually ceases to be linear and one must include terms proportional to $-t^2$. However, we know that by $t = L_T/v_{the}$, without the Biermann term, the magnetic field should saturate. We can thus estimate the final magnetic field as Eq. (2) at $t = L_T/v_{the}$, and arrive at the condition

$$\rho_e \approx L_n, \quad (3)$$

where $\rho_e \equiv v_{the}/\Omega_{ce}$ is the electron Larmor radius, and $\Omega_{ce} \equiv eB/m_e c$ is the electron cyclotron frequency. This can be rewritten in terms of the electron plasma beta, leading to the following scaling of the final magnetic field:

$$\frac{B}{\sqrt{8\pi P_e}} = \beta_e^{-1/2} \approx \frac{1}{\sqrt{2}}\frac{d_e}{L_n}, \quad (4)$$

where $d_e \equiv c/\omega_{pe}$ is the electron inertial length, and $\omega_{pe} \equiv \sqrt{4\pi n e^2/m_e}$ is the electron plasma frequency. For large L_n/d_e, which is typical of astrophysical systems and some experiments, this means B is small (β_e large), in other words the magnetic field generated can be considered insignificant.

The validity of Eq. (4) rests on the assumption that the Biermann term remains the dominant term in Eq. (1) as the magnetic field grows. Let us check that this is indeed true. The fluid velocity $\boldsymbol{v}$ should quickly reach the sound speed c_s. Assuming this flow, at $t = L_T/v_{the}$, the convection term scales as a factor of $\sqrt{m_e/m_i}$ smaller than the Biermann term and thus should remain negligible. (For simplicity, we have now assumed all gradients are of the same order $L \sim L_n \sim L_T$.) For small scales ($L < d_i$) the Hall term becomes stronger than the convection term. Because $\boldsymbol{j} = c\boldsymbol{\nabla} \times \boldsymbol{B}/4\pi$, at $t = L/v_{the}$ the Hall term scales as a factor of d_e^2/L^2 smaller than the Biermann term, and thus also should remain small as long as $L > d_e$.

A different situation arises if the density and temperature gradients are fixed, as may occur in a system with a long pulsed laser, i.e. one that continually supplies the Biermann term, or in astrophysical shocks which can also keep the gradients steady. In such cases, the convection term will eventually become significant. If we assume that there are no dynamo effects which cause the magnetic field to continue growing such that the convection term surpasses the Biermann term, these two terms may eventually balance as magnetic fields convect away from the Biermann source faster than the field can grow. This balance results in the following scaling for the saturated magnetic field strength:

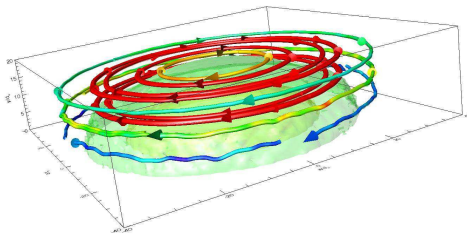$$\frac{B}{\sqrt{8\pi P_e}} = \beta_e^{-1/2} \approx \frac{1}{\sqrt{2}}\frac{d_i}{L}, \quad (5)$$

FIG. 1. A still frame (at $t\omega_{pe} = 235.2$, when the magnetic fields saturate) from a movie (multimedia view), showing the evolution of three contours of density, and a selection of magnetic field lines generated by the Biermann mechanism (from $t\omega_{pe} = 0$ to 298.2). This data is taken from the 3D simulation presented in Paper I[9] in which $L_T/d_e = 50$ with $m_i/m_e = 25$.

where $d_i \equiv c/\omega_{pi}$ is the ion inertial length, and $\omega_{pi} \equiv \sqrt{4\pi ne^2/m_i}$ is the ion plasma frequency, or equivalently $\rho_s \approx L$, where $\rho_s \equiv c_s/\Omega_{ce}$. As in Eq. (4), the final magnetic field scales as $1/L$.

This d_i/L scaling was predicted in previous works[10,11], including Haines[12], who also predicted that the saturated field would peak at $L/d_i \approx 1$ and vanish for small L/d_i. For these small, sub-d_i, scales the current is limited by microinstabilities such as the lower hybrid drift instability and the ion acoustic instability, which lead to a reduced magnetic field strength. This was confirmed for the first time in Paper I[9].

In Fig. 1 a still frame from a movie (multimedia view) is shown, which illustrates this generation of magnetic fields via the Biermann battery, with perpendicular temperature and density gradients in a 3D PIC simulation. The profiles generating these gradients are explained in section V. Three contours of density of the expanding plasma are displayed along with Biermann generated magnetic field lines at a time after the magnetic fields have grown and saturated. (This is from the 3D simulation presented in Paper I[9]; here, $L/d_e = 50$ and $m_i/m_e = 25$.) The movie shows the plasma expanding (at the sound speed) outward as magnetic fields are generated via the Biermann battery mechanism.

III. WEIBEL INSTABILITY

As we showed in Paper I[9], the configuration that gives rise to the Biermann Battery also triggers the Weibel instability[5] for $L/d_e > 100$. Note, only the temperature gradient is essential for this effect. This instability is caused by pressure anisotropies, and thus is an intrinsically kinetic effect. The anisotropy in this paper is due to the kinetic evolution of a temperature gradient in a collisionless system, the details of which will explained in a forthcoming publication. Unlike the Biermann battery,

the Weibel instability must start from a seed magnetic field. This seed field may be generated by the Biermann battery, or from small scale fluctuations found in both PIC simulations and in nature, due to finite numbers of particles (referred to as shot noise in electronics[13]).

To get a quantitative understanding of what is expected from such an instability, let us consider an initial plasma with a bi-Maxwellian velocity distribution:

$$f_{0\alpha} = n_\alpha v_{th\perp\alpha}^{-2} v_{th\|\alpha}^{-1} (2\pi)^{-3/2} \exp\left(-\frac{v_{\perp\alpha}^2}{2v_{th\perp\alpha}^2} - \frac{v_{\|\alpha}^2}{2v_{th\|\alpha}^2}\right),$$

$$(6)$$

where the thermal velocity is larger in one direction deemed as parallel $v_{th\|\alpha} > v_{th\perp\alpha}$, with $v_{th(\perp,\|)\alpha} \equiv \sqrt{T_{(\perp,\|)\alpha}/m_\alpha}$. The α index represents each of the particle species.

The dispersion relation of an unmagnetized collisionless plasma with this distribution can be obtained from the Vlasov equation. The solution for electromagnetic perturbations consists of the following expression[5]:

$$k_\perp^2 c^2 - \omega^2 - \sum_\alpha \omega_{p\alpha}^2 A_\alpha - \sum_\alpha \omega_{p\alpha}^2 (A_\alpha + 1) \xi_\alpha Z(\xi_\alpha) = 0$$

$$(7)$$

where $k_\perp$ is the wavenumber, $\omega_{p\alpha}$ is the plasma frequency, $A_\alpha \equiv T_{\|\alpha}/T_{\perp\alpha} - 1$ is the temperature anisotropy, $\xi_\alpha = \omega/\sqrt{2}k_\perp v_{th\perp\alpha}$, and $Z()$ is the plasma dispersion function[14]. For the purposes of this paper we assume that the ions do not play a role because of their large masses and low temperature and thus we will drop the α index; however, in systems with larger ion temperatures, they may play an important role on longer timescales, especially if the electron anisotropy is not present due to collisions. In this study, the instability is based on electron physics: the anisotropy is in the electron pressure, and the instability forms at the electron inertial scale d_e.

There exists a purely imaginary solution where $\omega = i\gamma$ as long as the normalized perturbation wavenumber $kd_e < \sqrt{A}$. This unstable growing mode is referred to as the Weibel instability, and is driven by the anisotropy A. Although we have described this instability in the context of a bi-Maxwellian distribution, similar physics is present for a wide range of velocity distributions with a larger velocity spread in the parallel direction. For example, delta functions[15], waterbag distributions[16], and kappa distributions[17] all yield similar solutions. We will later use the bi-Maxwellian solution to quantitatively check the growth rates and wavelengths found in our simulation.

IV. COMPUTATIONAL MODEL

Using the OSIRIS framework[18,19], we perform a set of particle-in-cell (PIC) simulations to investigate the generation and amplification of magnetic fields via the Biermann battery. We use the same initialization for our

simulations as in Paper I[9], a simplification of the afore-mentioned laser-plasma systems. The fluid velocity, electric field, and magnetic field are initially uniformly zero.

We start with a spheroid distribution of density, that has a shorter length scale in one direction:

$$n = \begin{cases} (n_0 - n_b)\cos(\pi R_1/2L_T) + n_b, & \text{if } R_1 < L_T, \\ n_b, & \text{otherwise,} \end{cases}$$

where $R_1 = \sqrt{x^2 + (L_T/L_n y)^2 + z^2}$,

(8)

n_0 is the reference density, and $n_b = 0.1n_0$ is a uniform background density. As in section II, the characteristic lengths of the temperature and density gradients are denoted by L_T and L_n, respectively. To represent the newly formed plasma bubble, which is flatter in the direction of the laser, z, we set $L_T/L_n = 2$ (this is a generic choice that appears to be qualitatively consistent with experiments, e.g.[20-22]; note, however, that the specific value of L_T/L_n depends on target and laser properties and thus can vary). Although this is the initial density, and can in principle change with time, it does not evolve much during our simulations: the density expands at the sound speed c_s and all simulations are run with $t \ll L_n/c_s$.

The initial velocity distributions are Maxwellian, with a uniform ion thermal velocity, v_{th0i}. The spatial profile for the electron thermal velocity is cylindrically symmetric along the z direction where it is hottest in the center. This is implemented in a similar manner to the density:

$$v_{the} = \begin{cases} (v_{th0e} - v_{thbe})\cos(\pi R_2/2L_T) + v_{thbe}, & \text{if } R_2 < L_T, \\ v_{thbe}, & \text{otherwise,} \end{cases}$$

where $R_2 = \sqrt{x^2 + z^2}$,

(9)

resulting in a maximum initial electron pressure, $P_{e0} = m_e n_0 v_{th0e}^2$. (Paper I[9] mistakenly stated $P_{e0} = m_e n_0 v_{th0e}^2/2$.) The numerical values of these thermal velocities are: $v_{th0e} = 0.2c$ and $v_{th0i} = v_{thbe} = 0.01c$. It is important to note that unlike the density profile, the temperature profile changes significantly with time: the peak drops by a factor of ~ 2, and the temperature gradient driving the Biermann battery vanishes after an electron transit time. This means we should expect agreement with Eq. (4) and not Eq. (5).

We will normalize the magnetic field for the results of this paper as $B/\sqrt{8\pi P_{e0}} = \beta_e^{-1/2}$, time as $t\omega_{pe}$ where $\omega_{pe} \equiv \sqrt{4\pi n_0 e^2/m_e}$, and distance as x/d_e where $d_e \equiv c/\omega_{pe}$. Unlike the previous definition of ω_{pe}, this uses the peak density n_0, so for regions where $n < n_0$, the local inverse electron beta, inverse plasma frequency, and electron inertial length are larger than the normalization indicates.

For simplicity the boundaries are periodic, but the box is large enough that they do not interfere with the dynamics. The dimensions of the simulation domain range from $-L, L$ in both x and y (and z in 3D), where
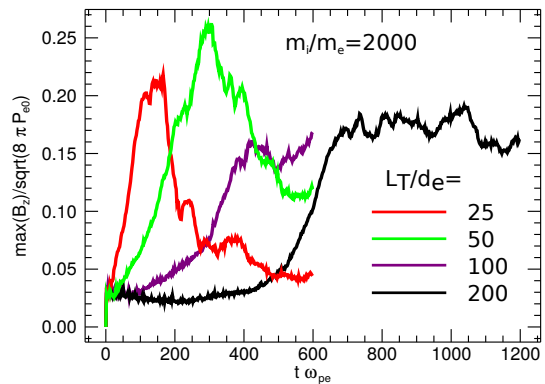

FIG. 2. Maximum magnetic field B_z vs. time for a selection of system sizes (L_T/d_e) with $m_i/m_e = 2000$. This figure shows the same qualitative behavior as figure 3(a) in Paper I[9]. The results of the simulation with $L_T/d_e = 400$ are presented in Fig. 8.

$L = 15/8L_T$. The spatial resolution is 8 grid points/d_e or 1.6 grid points/λ_d, where λ_d is the Debye length (This resolution is the same as that used in Paper I[9], which mistakenly reported 16 grid points/d_e). The time resolution is $\Delta t\omega_{pe} = 0.07$. The 2D simulations have 64 particles per grid cell (ppg), and the 3D simulation has 27 ppg.

V. INSENSITIVITY TO MASS RATIO

In order to investigate a larger range of L_T/d_i, the simulations presented in Paper I[9] were run with a reduced mass ratio of 25. In order to test the dependence of the values reported there on mass ratio, we simulate with a mass ratio of 100, 400, and the more realistic 2000. (In most astrophysical contexts, the mass ratio would be the 1836 of Hydrogen, while laser experiments have a larger value.)

In Fig. 2, the maximum magnetic field is displayed versus time for various system sizes, L_T/d_e. This plot is equivalent to Figure 3(a) in Paper I[9], now using a realistic mass ratio of $m_i/m_e = 2000$. There is no qualitative difference between the realistic mass and the simulations done in Paper I[9] with $m_i/m_e = 25$. For the simulations with $L_T/d_e = 25$ and 50, the magnetic field strength reaches a peak and decays away due to the ion acoustic instability[12]. This instability is stronger at larger mass ratio, and thus still relevant at the larger $L_T/d_e = 50$. For $L_T/d_e = 100$ and 200, the magnetic field saturates around its peak value. These are equivalent to the results found for $m_i/m_e = 25$. The growth of the field occurs about 8 times faster than predicted in Eq. (2). This is an effect of our particular choice of a density profile. The derivation of Eq. (2) assumes $\boldsymbol{\nabla}n/n = 1/L_n$, while more precisely $\boldsymbol{\nabla}n/n = n_0/n(\boldsymbol{x})L_n$, and for our profile
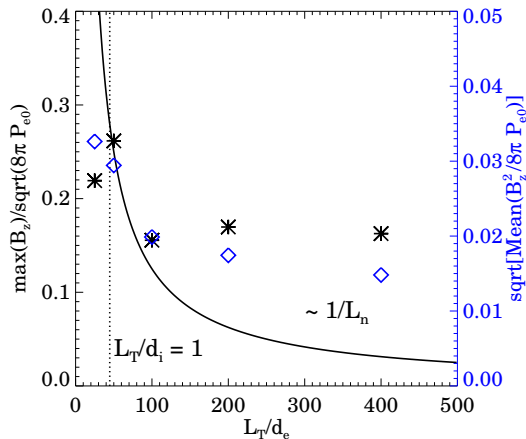
FIG. 3. Maximum (black asterisks), and average magnitude (blue diamonds) of the magnetic field, B_z, vs. L_T/d_e with $m_i/m_e = 2000$ at the time, $t\omega_{pe}$, when the magnetic field reaches a maximum. The solid black curve indicates a scaling of $\sim 1/L_n$ (exactly $6.25d_e/L_n$), and the dotted line indicates where $L_T/d_i = 1$.

$n_0/n(\boldsymbol{x}) = 8$ at the location of fastest magnetic field growth.

In Fig. 3 we present the scaling of maximum and average magnitude (the square root of B_z^2 averaged in a box $2L_T \times 2L_n$ surrounding the expanding bubble) of the saturated magnetic field (or peak magnetic field for $L_T/d_e \leq 50$) as a function of system size. This is equivalent to Figure 3(b) in Paper I[9], but with $m_i/m_e = 2000$. Much like the $m_i/m_e = 25$ case, Fig. 3 shows three regions; one where the Biermann magnetic field growth is suppressed by microinstabilities (the peak field is suppressed for $L/d_e = 25$), a regime that scales as d_e/L_T ($\approx 8d_e/\sqrt{2}L_T \approx 6.25d_e/L_T$) after a peak around $L_T/d_i = 1$, and a Weibel dominated regime for $L/d_e \geq 100$. In contrast to the purely Biermann prediction where the saturated magnetic field vanishes at large L_T, in the Weibel dominated regime the saturated magnetic field strength remains finite for large system sizes, confirming the conclusions obtained for $m_i/m_e = 25$ in Paper I[9]. The numerical trends shown in Fig. 3 suggest that the magnetic field amplitude at saturation in the Weibel regime is independent of L_T. This is compatible with existing understanding on the saturation of the Weibel instability[23–25]. The presented magnitude of the saturated magnetic field is slightly larger than shown in Paper I[9] ($\beta_e \approx 32$ instead of 100) (see also Fig. 5). Note that at the location of maximum B, the local thermal velocity is close to $1/2v_{th0e}$ and the local density close to $1/4n_0$. Therefore, the value of β_e at that location is $\beta_e \approx 2$.

The distinction between the Weibel and Biermann regimes is evident where the saturated magnetic field strength stops following the d_e/L_T scaling, but it can be more clearly seen when observing the structure of the magnetic fields in space for each simulation. A plot of
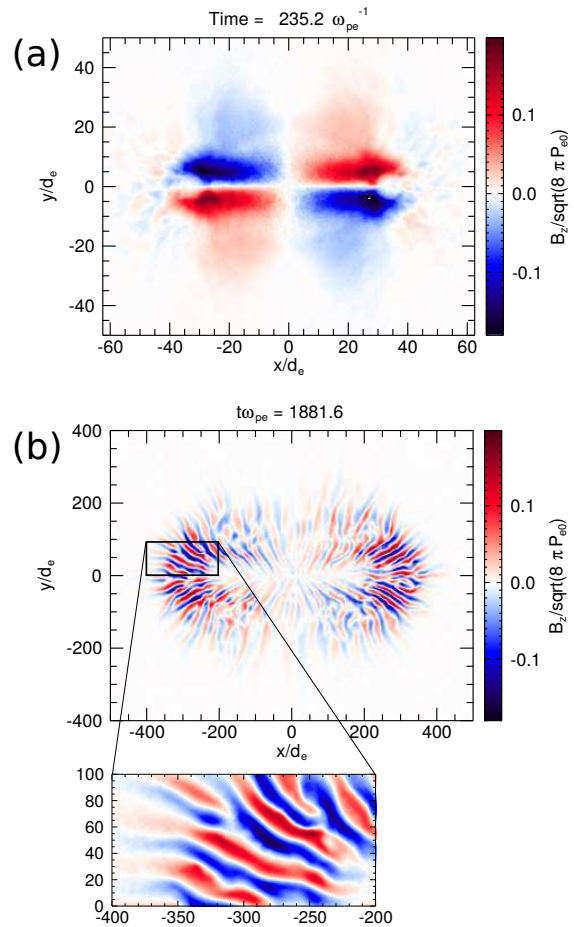

FIG. 4. Out-of-plane magnetic field B_z at peak magnitude with $m_i/m_e = 2000$ for, (a) $L_T/d_e = 50$ (Biermann regime) at $t\omega_{pe} = 235.2$, and (b) $L_T/d_e = 400$ (Weibel regime) at $t\omega_{pe} = 1881.6$, and zoom-in of Weibel fields showing $kd_e \approx 0.2$ (wavelength $\lambda/d_e \approx 31.4$).

the out-of-plane magnetic field is shown in Fig. 4, for $L_T/d_e = 50$, and 400. In the Biermann regime, shown in Fig. 4(a) ($L_T/d_e = 50$), the spatial structures of the magnetic field are at the system size, and follow the structures of the initial density and temperature profiles. The Weibel regime, on the other hand, seen in Fig. 4(b) ($L_T/d_e = 400$), exhibits small ($kd_e \approx 0.2$) magnetic structures consistent with the Weibel instability. These observations are qualitatively the same as shown in Figure 2 of Paper I[9]. The length scale of the initial Weibel filaments is also consistent with the magnetic spectra, which is presented (for $m_i/m_e = 25$) in Figure 5 of Paper I[9] showing a peak at $kd_e \approx 0.2$.

Assuming the mass ratio is sufficiently large, the Weibel instability is independent of mass ratio, because it is based on electron dynamics that act at timescales much faster than the ions. We thus expect the saturated magnetic field to asymptote as the mass ratio increases. To verify this we performed a scan in mass ratio for the
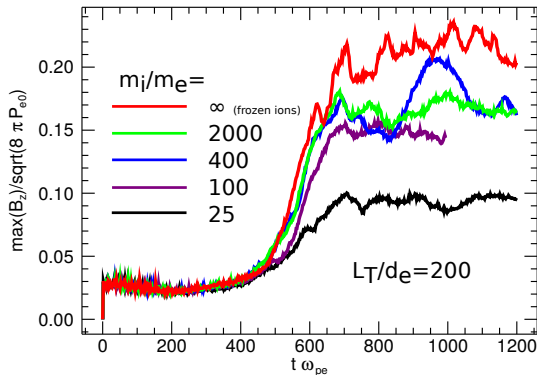
FIG. 5. Maximum magnetic field B_z *vs.* time for a selection of mass ratios (m_i/m_e) at $L_T/d_e = 200$ (Weibel regime).

$L_T/d_e = 200$ case, which is in the Weibel regime, but computationally small enough to perform several simulations. In Fig. 5 we show that the magnitude of the magnetic field is only weakly dependent on the mass ratio. Although it changes in magnitude by a factor of 2 from $m_i/m_e = 25$ to 100, with larger mass ratios the saturated magnetic field appears to asymptote. There is little difference even for frozen ions where the effective mass ratio is infinite. In addition, we find that the length scales of the magnetic perturbations are insensitive to mass ratio.

VI. EVIDENCE FOR THE WEIBEL INSTABILITY

In Paper I[9] we have shown evidence of the development of the Weibel instability in simulations of expanding plasmas with perpendicular temperature and density gradients. Here we further show that the simulation results exhibit excellent agreement with theoretical predictions of both the growth rate and wavenumber for the Weibel instability.

Looking at the time evolution of the growth of the magnetic fields, we are able to measure the growth rate of the instability producing the small scale magnetic fields ($kd_e \approx 0.2$) observed in our simulations. In Fig. 6, for the $L_T/d_e = 400$ simulation where we claim the magnetic fields are dominated by the Weibel instability, the measured growth rate of the maximum and average magnetic field is $\gamma/\omega_{pe} = 0.007$, and 0.006 respectively. We find the same measured growth rate for both the smaller mass ratio $m_i/m_e = 25$ shown in Fig. 6(a), and the more realistic $m_i/m_e = 2000$ in Fig. 6(b), consistent with our expectation that the plasma dynamics we are observing are due to the electrons, not the ions.

We can test these observed growth rates and wavenumbers by comparing their values to that predicted by theory, namely, the fastest growing mode calculated from Eq. (7). This is only a rough estimate of the instability because there are density and temperature gra-
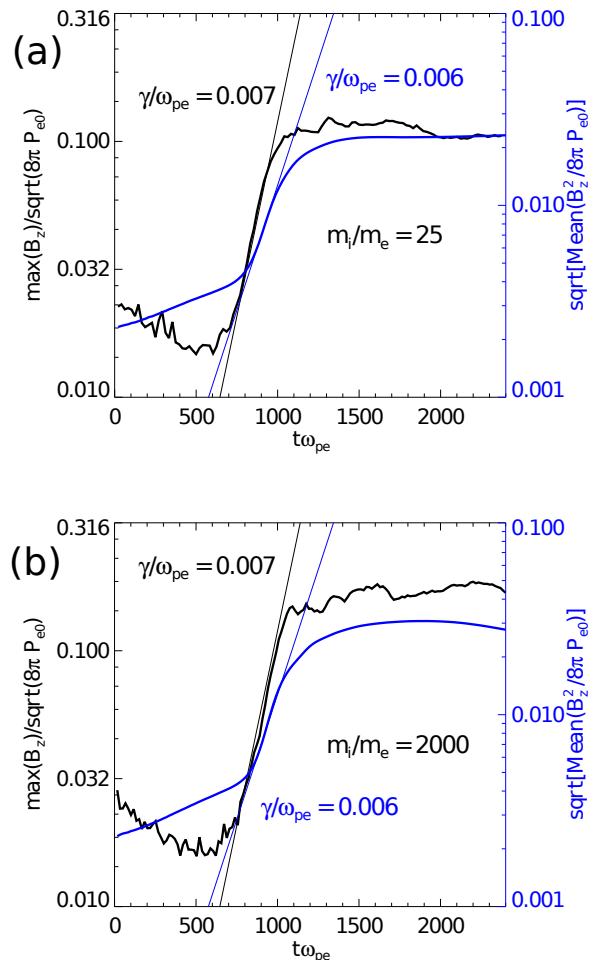

FIG. 6. Maximum (black curve) and average magnitude (blue curve) of magnetic field B_z *vs.* time for $L_T/d_e = 400$, with $m_i/m_e =$ (a) 25, and (b) 2000. This plot shows the respective growth rates (of the instability identified as the Weibel instability) corresponding to $\gamma/\omega_{pe} = 0.007$ and 0.006.

dients in the simulation, and the velocity distributions have evolved, and are likely not bi-Maxwellian. However, these factors should not significantly influence the result. As stated in section III, similar solutions exist for a variety of distribution functions, and at the scale of the Weibel instability, the variation of temperature and density due to the background gradients is negligible. The parameters of Eq. (7) are: A, $v_{th\perp e}$, and the local plasma frequency ω_{pe}, which depends on the local plasma density n. One of the outputs of OSIRIS is the thermal spread (of the electrons) in the x and y directions, v_{thex} and v_{they}. This allows us to measure $A = v_{th\|e}^2/v_{th\perp e}^2 - 1$ along $y = 0$ where $v_{thex} = v_{th\|e}$, and $v_{they} = v_{th\perp e}$. In addition, we measure n so that we can solve the dispersion relation numerically from Eq. (7) at each position along x. We calculate the predicted γ for a range of k, so that we can obtain the fastest growing γ and the associated k.

In Fig. 7 we show a plot of the measured anisotropy A, and the calculated γ and k of the fastest growing
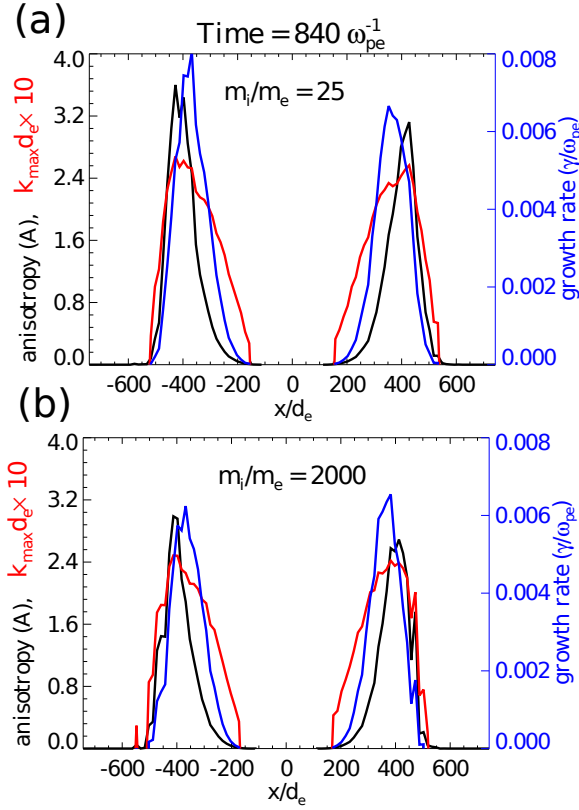
FIG. 7. Anisotropy (A) (black curve), $k_{max}d_e$ (red curve), and growth rate (γ/ω_{pe}) of the Weibel instability as predicted from Eq. (7) (blue curve), along a cut at $y = 0$ at $t\omega_{pe} = 840$ for $L_T/d_e = 400$, with $m_i/m_e =$ (a) 25, and (b) 2000.
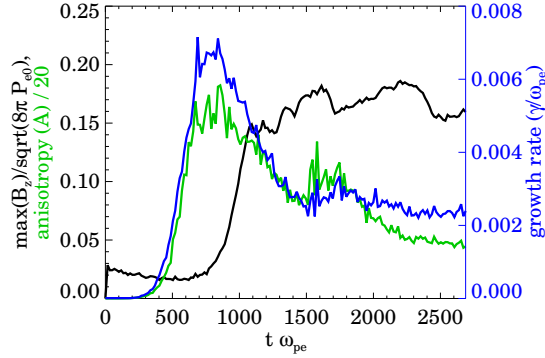

FIG. 8. Maximum magnetic field B_z (black curve), anisotropy (A)/20 (green curve), and growth rate (γ/ω_{pe}) of the Weibel instability as predicted from Eq. (7) (blue curve), versus time for $L_T/d_e = 400$, with $m_i/m_e = 2000$.

mode, along $y = 0$ at $t\omega_{pe} = 840$. This is during the time with the largest growth rate γ ($t\omega_{pe} \approx 700 - 1100$, see Fig. 8). Again we find almost equivalent results for the smaller mass ratio $m_i/m_e = 25$ shown in Fig. 7(a), and the more realistic $m_i/m_e = 2000$ in Fig. 7(b). The maximum growth rate along x is $\gamma/\omega_{pe} \approx 0.007$, which
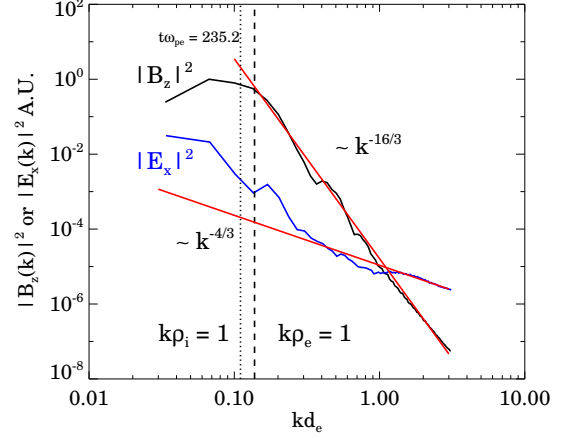

FIG. 9. The energy spectrum of the magnetic field B_z (black curve), and electric field E_x (blue curve), for the 3D simulation ($L_T/d_e = 50$ and $m_i/m_e = 25$) at $t\omega_{pe} = 235.2$ (when the magnetic field growth saturates). The dotted line indicates where $k\rho_i = 1$, and the dashed line where $k\rho_e = 1$, below which power law behaviors are predicted, with a slope of $-16/3$ for magnetic energy, and $-4/3$ for electric energy, as shown in the solid red curves[26]. [Note that in this simulation $\rho_i \sim \rho_e$ because the temperature ratio $T_e/T_i = 16$ is comparable to the mass ratio.]

is consistent with the values measured above in Fig. 6. In addition, the calculated $kd_e \approx 0.2$ matches the observations, and the locations with the largest growth rate ($|x/d_e| \approx 200 - 400$) are coincident with the Weibel fields visible in Fig. 4(b), and Figure 2(b) of Paper I[9].

In Fig. 8, like in Fig. 2, we show the maximum magnetic field versus time, now for $L_T/d_e = 400$. In addition we show the maximum measured anisotropy A across x (green curve), and the maximum calculated growth rate γ (blue curve). The growth rate γ increases with A, and peaks at the same time as the magnetic field begins to grow, strongly suggesting the Weibel instability.

To summarize, there is strong evidence that the Weibel instability is generated in our simulations; the growth rate, wavenumber, and the location and time where the fastest growth of the measured instability occur, are consistent with the theoretical predictions.

VII. GYROKINETIC POWER LAW SPECTRA

A surprising finding in Paper I[9] was the agreement of the power law slope of the magnetic energy spectrum at scales below the electron Larmor radius, with gyrokinetic predictions[26]. The prediction is based on energy transferred via a turbulent cascade of kinetic Alfvén waves, which is converted at $k\rho_e \sim 1$ via electron Landau damping into an entropy cascade.

For the 3D run that was reported in Paper I[9], where $L_T/d_e = 50$, the dominant magnetic field is generated

by the Biermann battery. This magnetic field (shown in Fig. 1) acts as a guide field on which kinetic Alfvén waves may propagate, damp, and generate the predicted cascade.

In Fig. 9, we show the magnetic and electric energy spectra for this run. The spectra are obtained by performing a Fourier transform over the entire system for one component of the electric or magnetic fields, and then averaging over all directions of $\boldsymbol{k}$. In addition to the $-16/3$ power-law slope of the magnetic energy already revealed in Paper I[9], we observe that the electric energy spectrum is in good agreement with a $-4/3$ power-law, as predicted[26]. At the time shown, the spectra has reached a steady state and remains unchanged for the rest of the simulation, up to $t\omega_{pe} = 298.2$.

VIII. CONCLUSIONS

We have performed kinetic simulations of plasmas with perpendicular temperature and density gradients of ranging mass ratio up to $m_i/m_e = 2000$, and confirmed the magnetic field generation and amplification shown in Paper I[9]. We have shown that as the system size increases beyond $L_T/d_e \sim 100$, the major source of magnetic field changes from the Biermann battery mechanism to kinetic Weibel generated fields, which remain finite ($\beta_e \sim 1$) for large system sizes. We have done further analysis on the simulations done in Paper I[9], and on the new simulations with $m_i/m_e = 2000$ confirming that in large system sizes, magnetic fields are generated by the Weibel instability. Finally we have shown that our results agree with gyrokinetic models in power laws found in both electric and magnetic energy spectra.

We reiterate the main applications of our conclusions shown in Paper I[9], which are significant to the topic of the generation of magnetic fields in astrophysical contexts including shocks found in supernova remnants. Although small scale, the Weibel instability generates magnetic fields at significant levels ($\beta_e \sim 1$ independent of L_T). These are astrophysically relevant magnitudes in typical contexts (where $L_T/d_i \gg 1$), unlike the fields predicted by the Biermann battery that yield $\beta_e \sim (d_i/L_T)^{-2}$. However the discrepancy between the large scales of astrophysical magnetic fields and the microscopic Weibel fields remains. Whether it is possible for a mechanism such as turbulence to bridge this gap remains an outstanding mystery of astrophysical research.

The matching of power law spectra points to the exciting possibility of validating theories of kinetic turbulence in laser experiments. Due to the small scale separation between L_T, ρ_i, and ρ_e in our 3D simulation, we are only able to measure a sub-ρ_e power law. However, the spectra at other scales could potentially be tested in simulations and experiments. In addition to the configuration that we have studied, Weibel-generated turbulence may occur due to anisotropies induced by other mechanisms; for example, laser-generated hot electron beams

with return currents. It might be possible to probe such magnetized laser plasmas in order to investigate turbulence at kinetic scales. Indeed, one such an experiment has recently been performed at the Tata Institute of Fundamental Research, Mumbai[27], probing the magnetic energy spectra in the range with $\rho_i^{-1} \lesssim k < \rho_e^{-1}$. A power law of $-7/3$ has been measured from the experimental results (to be published shortly), consistent with theoretical predictions[26].

In existing (and future) laser-plasma experiments the predicted $1/L$ scalings in Eq. (4) and Eq. (5) of the saturated Biermann magnetic fields should be relevant. Furthermore, it may be possible to find the electron-Weibel instability as we have done here, as long as collisions do not occur faster than the electron transit time and keep the temperature isotropic ($\nu_{ei}L_T/v_{the} \ll 1$). Based on experimentally relevant parameters, this condition is equivalent to the following engineering formula:

$$1\times10^{-2}\left(\frac{n}{1 \times 10^{19}\ \mathrm{cm}^{-3}}\right)\left(\frac{\ln\Lambda}{10}\right)\left(\frac{L_T}{400\mu m}\right)\left(\frac{T_e}{1\mathrm{keV}}\right)^{-2} \ll 1,$$
(10)

where n is the number density, $\ln\Lambda$ is the Coulomb logarithm, L_T is the gradient scale, and T_e is the electron temperature. This inequality suggests the possibility of observing the Weibel instability, since the physical values quoted above are reasonable numbers which can occur at the low density, high temperature coronae generated around laser targets, e.g.[28]. Note that in this work the strong temperature gradient is assumed to form before the anisotropy and the subsequent instability. We think this is a good modeling assumption in cases where intense short-pulse lasers are used. Cases with longer, less intense lasers require more careful consideration due to the possible influence of collisions and the laser fields during the timescale of the experiment.

IX. ACKNOWLEDGMENTS

[1] R. M. Kulsrud and E. G. Zweibel, Rep. Prog. Phys. **71**, 046901 (2008).
[2] R. M. Kulsrud and S. W. Anderson, Astrophys. J. **396**, 606 (1992).
[3] A. Brandenburg, D. Sokoloff, and K. Subramanian, Space Sci. Rev. **169**, 123 (2012).
[4] L. Biermann, Z. Naturforsch. **5a**, 65 (1950).

[5] E. S. Weibel, Phys. Rev. **114**, 18 (1959).

[6] J. A. Stamper, K. Papadopoulos, R. N. Sudan, S. O. Dean, and E. A. McLean, Phys. Rev. Lett. **26**, 1012 (1971).

[7] C. K. Li, F. H. Séguin, J. A. Frenje, J. R. Rygg, R. D. Petrasso, R. P. J. Town, P. A. Amendt, S. P. Hatchett, O. L. Landen, A. J. MacKinnon, *et al.*, Phys. Rev. Lett. **97**, 135003 (2006).

[8] L. Gao, P. M. Nilson, I. V. Igumenshchev, M. G. Haines, D. H. Froula, R. Betti, and D. D. Meyerhofer, Phys. Rev. Lett. **114**, 215003 (2015).

[9] K. M. Schoeffler, N. F. Loureiro, R. A. Fonseca, and L. O. Silva, Phys. Rev. Lett. **112**, 175001 (2014).

[10] C. E. Max, J. J. Thomson, and W. M. Manheimer, Phys. Fluids **21**, 128 (1978).

[11] R. S. Craxton and M. G. Haines, Plasma Phys. **20**, 487 (1978).

[12] M. G. Haines, Phys. Rev. Lett. **78**, 254 (1997).

[13] W. Schottky, Ann. Phys. **362**, 541 (1918).

[14] B. D. Fried and S. D. Conte, *The Plasma Dispersion Function* (Academic Press, New York, 1961).

[15] B. D. Fried, Phys. Fluids **2**, 337 (1959).

[16] P. H. Yoon and R. C. Davidson, Phys. Rev. A **35**, 2718 (1987).

[17] S. Zaheer and G. Murtaza, Phys. Plasmas **14**, 022108 (2007).

[18] R. A. Fonseca, L. O. Silva, F. S. Tsung, V. K. Decyk, W. Lu, C. Ren, W. B. Mori, S. Deng, S. Lee, T. Katsouleas, and J. C. Adam, Lect. Notes Comput. Sci. **2331**, 342 (2002).

[19] R. A. Fonseca, S. F. Martins, L. O. Silva, J. W. Tonge, F. S. Tsung, and W. B. Mori, Plasma Phys. Contr. Fusion **50**, 124034 (2008).

[20] P. M. Nilson, L. Willingale, M. C. Kaluza, C. Kamperidis, S. Minardi, M. S. Wei, P. Fernandes, M. Notley, S. Bandyopadhyay, M. Sherlock, R. J. Kingham, M. Tatarakis, Z. Najmudin, W. Rozmus, *et al.*, Phys. Rev. Lett. **97**, 255001 (2006).

[21] C. K. Li, F. H. Seguin, J. A. Frenje, J. R. Rygg, R. D. Petrasso, R. P. J. Town, O. L. Landen, J. P. Knauer, and V. A. Smalyuk, Phys. Rev. Lett. **99**, 055001 (2007).

[22] N. L. Kugland, D. D. Ryutov, P.-Y. Chang, R. P. Drake, G. Fiksel, D. H. Froula, S. H. Glenzer, G. Gregori, M. Grosskopf, M. Koenig, Y. Kuramitsu, C. Kuranz, M. C. Levy, E. Liang, *et al.*, Nat. Phys. **8**, 809 (2012).

[23] R. C. Davidson, D. A. Hammer, I. Haber, and C. E. Wagner, Phys. Fluids **15**, 317 (1972).

[24] F. Califano, F. Pegoraro, S. V. Bulanov, and A. Mangeney, Phys. Rev. E **57**, 7048 (1998).

[25] L. O. Silva, R. A. Fonseca, J. W. Tonge, J. M. Dawson, W. B. Mori, and M. V. Medvedev, Astrophys. J. Lett. **596**, L121 (2003).

[26] A. A. Schekochihin, S. C. Cowley, W. Dorland, G. W. Hammett, G. G. Howes, E. Quataert, and T. Tatsuno, Astrophys. J. Suppl. Ser. **182**, 310 (2009).

[27] S. Mondal, V. Narayanan, W. J. Ding, A. D. Lad, B. Hao, S. Ahmad, W. M. Wang, Z. M. Sheng, S. Sengupta, P. Kaw, A. Das, and G. R. Kumar, Proc. Nat Acad. Scai. U.S.A. **109**, 8011 (2012).

[28] L. Gao, P. M. Nilson, I. V. Igumenschev, G. Fiksel, R. Yan, J. R. Davies, D. Martinez, V. Smalyuk, M. G. Haines, E. G. Blackman, D. H. Froula, R. Betti, and D. D. Meyerhofer, Phys. Rev. Lett. **110**, 185003 (2013).